Structural and electronic characteristics of amorphous $Ge_8Sb_2Te_{11}$

Chong Qiao[1], Yujun Niu[1], Shengzhao Wang[1], Rongchuan Gu[2], Qundao Xu[2], Chao Chen[3,*], Songyou Wang[4], Cai-Zhuang Wang[5], Ming Xu[2,*] and Xiangshui Miao[2]

[1]*School of Mathematics and Physics, Nanyang Institute of Technology, Nanyang 473004, China*
[2]*School of Integrated Circuits, Huazhong University of Science and Technology, Wuhan 430074, China*
[3]*School of Physical and Mathematical Sciences, Nanjing Tech University, Nanjing 211816, China*
[4]*Shanghai Ultra-Precision Optical Manufacturing Engineering Center and Department of Optical Science and Engineering, Fudan University, Shanghai 200433, China*
[5]*Ames Laboratory, U. S. Department of Energy and Department of Physics and Astronomy, Iowa State University, Ames, Iowa 50011, USA*

*E-mail address: chenchao@njtech.edu.cn and mxu@hust.edu.cn

Abstract

GeTe-rich phase-change materials can be utilized in rewriteable optical memory due to the large contrast in reflectivity between amorphous and crystalline phases. Here we explored the structure and electronic properties of amorphous $Ge_8Sb_2Te_{11}$ using *ab initio* molecular dynamics simulations. The results indicate that amorphous $Ge_8Sb_2Te_{11}$ is dominantly composed of Ge-, Sb- and Te-centered octahedrons with distortions, while 30.4% of Ge-centered clusters are in the form of tetrahedrons which are randomly distributed. The 5-fold rings possess a large proportion, and the Ge-Te and Sb-Te bonds present larger formation energies than other bonds, leading to the ABAB bonding sequence (A: Ge and Sb, B: Te). The lone pair electrons locating at the opposite direction of bonds possess a large fraction of 14.8%, which may enhance the distortions of local clusters. These structural properties lead to the high stability of amorphous $Ge_8Sb_2Te_{11}$ and thus long data retention in the information storage.

Keywords: amorphous $Ge_8Sb_2Te_{11}$; local structure; electronic property; molecular dynamics

Introduction

Phase-change materials (PCMs) are widely utilized as the medium of the emerging non-volatile phase-change memory and optical data storage devices, owing to the rapid and reverse transition between amorphous and crystalline phases accompany with the large contrast in resistivity and reflectivity [1-6]. PCMs are dominantly originated from the Ge-Sb-Te alloys locating at the pseudo-binary line between GeTe and Sb_2Te_3 [7-9]. The Sb_2Te_3-rich PCMs such as $Ge_2Sb_2Te_5$ and $GeSb_2Te_4$ are usually used for the high-speed phase-change memory as they present fast crystallization behavior [10,11]. In addition to the universal rapid phase-change behavior, the GeTe-rich PCMs not only present the high amorphous stability but also possess the large bandgap. Moreover, the optical reflectivity between the two phases monotonically increases with the GeTe content in the infrared spectral range, thus the GeTe-rich PCMs also hold a significant potential for optical metamaterials [12].

Amorphous $Ge_8Sb_2Te_{11}$ is a typical GeTe-rich PCM with the high stability and large reflectance contrast [13,14]. The crystalline $Ge_8Sb_2Te_{11}$ is in a Peierls-distorted rock-salt structure [15,16], in which one sublattice is occupied with Te and the other one is occupied with a random distribution of Ge, Sb, and vacancies [17], forming the defective octahedron in local configuration [18]. The local clusters in amorphous $Ge_8Sb_2Te_{11}$ tend to form octahedral configurations, but part of Ge-centered clusters can also form tetrahedrons [19]. As the amorphous phases contain nuclei with high similarity in local structure to crystals, they can achieve the fast and reverse phase transition [20]. Note that the simulation or preparation methods of the amorphous state also have an influence on the local structures, for example, the as-deposited phase has more tetrahedrons and homopolar bonds than the melt-quenched sample [21,22]. As-deposited amorphous $Ge_8Sb_2Te_{11}$ is more stable than as-deposited amorphous $Ge_2Sb_2Te_5$, while pressure-amorphized $Ge_8Sb_2Te_{11}$ is less stable than the pressure-amorphized $Ge_2Sb_2Te_5$ [23]. Kim et al. reported that the hydrogenation could effectively inhibits the transition of amorphous $Ge_2Sb_2Te_5$ but hardly affected that of amorphous $Ge_8Sb_2Te_{11}$ [24]. And Song et al. noticed that the crystallization speed was

largely improved by adding Ag in $Ge_2Sb_2Te_5$ but not in $Ge_8Sb_2Te_{11}$ [25]. These study indicates that amorphous $Ge_8Sb_2Te_{11}$ possesses a high stability. To improve the higher crystallization temperature of amorphous $Ge_8Sb_2Te_{11}$, Koch et al. demonstrated that the substitution of Ge by Sn can decrease the crystallization temperature [26]. And Zalden et al. found that the substitution of Ge by Sn also could speed up the crystallization kinetics [16]. Usually, the optical and electronic properties change with the structure. Buller et al. claimed that the reflectivity contrast between amorphous and crystalline phases can be increased by partial substitution of Te by Se and Ge by Sn [27]. Wang et al. clarified that the reflectivity contrast also can be improved by reducing the vacancy concentration [28]. Although these early investigations have explored the structure and optical property of the amorphous $Ge_8Sb_2Te_{11}$, the understanding of the local structure is still very limited up to date.

In the work, we have investigated the structural, dynamics, bonding and electronic properties of amorphous $Ge_8Sb_2Te_{11}$ by using ab initio molecular dynamics (AIMD) simulations. During the cooling process, the short-range order (SRO) is enhanced and the medium-range order (MRO) is formed gradually. Our analysis indicates that the SRO is ascribed to the large fraction of Ge-, Sb- and Te-centered octahedral structures and the relatively small fraction of Ge-centered tetrahedrons, while the MRO is characterized by the connection of these SROs. With the decreasing temperature, the evolution of vibrational frequency of the local structure is also explored to identify the relation between the vibrational frequency and local structure. Moreover, the formation energies of different bonding configurations are studied to analyze the bonding nature in amorphous $Ge_8Sb_2Te_{11}$. Additionally, the electronic property is investigated to unveil the photoelectric behavior. The research results enrich the knowledge of amorphous $Ge_8Sb_2Te_{11}$, which can effectively speed up the design and application in photoelectric devices.

Methods

The AIMD simulations were performed to simulate the amorphization process of

$Ge_8Sb_2Te_{11}$, with the Vienna Ab initio Simulation Package (VASP) code based on the density functional theory (DFT) [29,30]. The projector augmented-wave (PAW) method and Perdew-Burke-Ernzerhof generalized gradient approximation (GGA-PBE) were used for the exchange correlation functional [31,32]. Similar to our previous studies [33-35], the amorphous phase is usually obtained by a melt-quenching method. Firstly, the initial model was built in a cubic box, which was composed of 80 Ge, 20 Sb and 110 Te atoms. Secondly, the model was heated to 3000 K and relaxed for a long time to eliminate the memory effect from the initial position. Then, the liquid model was cooled gradually to 300 K, with a cooling rate of 33.3 K/ps, and the configurations at different temperatures were sampled. Note that the box was adjusted to ensure the pressure close to zero. Finally, the atomic trajectory was utilized to analyze to structure and dynamics characteristics. During the AIMD simulations, the time step was 3 fs, only one Γ point was selected from the Brillouin zone, and the canonical (NVT) ensemble was used to adjust the temperature and pressure [36,37]. The atomic number density of amorphous $Ge_8Sb_2Te_{11}$ is about 0.0295 $Å^{-3}$, which is close to the experimental value (0.0311 $Å^{-3}$) [13]. As for the electronic property, the energy cutoff was 500 eV, the amorphous $Ge_8Sb_2Te_{11}$ was optimized at 0 K with a force convergence of 0.02 eV, and the Brillouin zone was sampled with a 2 × 2 × 2 k-points grid.

Results and discussion

The total pair correlation function g(r) of amorphous $Ge_8Sb_2Te_{11}$ in the cooling process is shown in Fig. 1(a), which characterizes the amorphous structure based on the atomic distance. As the temperature decreases, the first peak located at ~2.79 Å becomes sharper and its altitude is obviously increased, suggesting that the short-range order (SRO) in amorphous $Ge_8Sb_2Te_{11}$ is enhanced. The second peak is observed at ~4.18 Å, and also increases with the decreasing temperature, indicating the formation of medium-range order (MRO). Beyond 6 Å, the g(r) changes little with the temperature, hinting that there is no long-range order in amorphous $Ge_8Sb_2Te_{11}$. The height of the second peak is much smaller than that of the first peak, demonstrating that the

amorphous $Ge_8Sb_2Te_{11}$ is composed of the strong SRO and weak MRO. These structure configurations are similar to the other PCMs [38,39].

The partial g(r) of amorphous $Ge_8Sb_2Te_{11}$ are shown in Fig. 1(b). The peaks of Sb-Sb, Ge-Te and Sb-Te configurations are very prominent in the first atomic shell, locating at 2.89 Å, 2.79 Å and 2.89 Å, respectively. It indicates that Ge atoms tend to bond with Te atoms while Sb atoms could bond with both Sb and Te atoms in amorphous $Ge_8Sb_2Te_{11}$. The peaks of Ge-Ge, Ge-Sb and Te-Te configurations are relatively small, locating at 2.60 Å, 2.79 Å and 2.98 Å, respectively. It reveals that the amount of Ge-Ge, Ge-Sb and Te-Te bonds are very limited in amorphous $Ge_8Sb_2Te_{11}$.

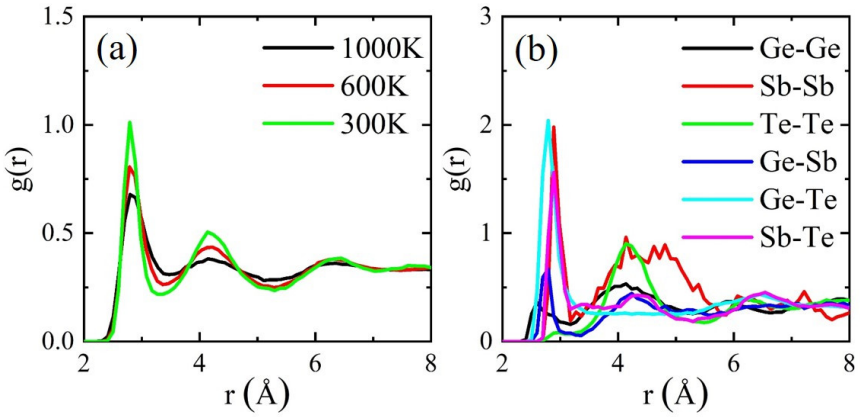

Fig. 1 The total g(r) (a) of amorphous $Ge_8Sb_2Te_{11}$ at different temperatures and partial g(r) (b) of amorphous $Ge_8Sb_2Te_{11}$ at 300 K.

To explore the local bonding environment, the coordination numbers (CNs) of Ge, Sb and Te atoms are calculated for amorphous $Ge_8Sb_2Te_{11}$ under different temperatures, as shown in Fig. 2(a). At 1000 K, the CNs of Ge, Sb and Te elements are 3.89, 3.27 and 2.73, respectively. When the temperature decreases to 300 K, the CNs change to 3.87, 3.10 and 2.82, respectively. It indicates that the CNs of Ge and Sb decrease while that of Te increases in the cooling process. The CNs of Ge and Te are close to the previous results reported by Akola et al. [19], but the CN of Sb shows an obvious discrepancy. This is probably due to the different pressure regulation in the amorphization simulation. Fig. 2(b) shows the CN of Ge-centered configurations, in which the Ge-Te configuration possesses a large fraction while the Ge-Ge and Ge-Sb configurations possess a relatively small proportion. As the temperature decreases, the CN of Ge-Te

configurations gradually increases while those of Ge-Ge and Ge-Sb configurations decrease. Fig. 2(c) shows the CN of Sb-centered configurations, which is composed of a large fraction of Sb-Te configuration and a small fraction of Sb-Ge and Sb-Sb configurations. As the temperature decreases, the CN of Sb-Te configuration changes little, the CN of Sb-Sb configuration shows a little increment while that of Sb-Ge configuration decreases gradually. Fig. 2(d) shows the CN of Te-centered configurations, which is dominantly made up of Te-Ge configuration. With the decreasing temperature, the CN of Te-Sb configuration changes little, the CN of Te-Ge configuration increases while that of Te-Te configuration decreases. In amorphous Ge-Sb-Te alloys, Ge and Sb are usually seen as cation while Te is seen as anion, thus the Ge-Ge, Ge-Sb, Sb-Sb and Te-Te configurations form the wrong bonds [40,41]. From Fig. 2(b)-(d), the amorphous $Ge_8Sb_2Te_{11}$ is mainly in the form of Ge-Te and Sb-Te configurations, forming the ABAB bonding alternations (A: Ge, Sb, B: Te) [42,43], and they are enhanced in the amorphization process.

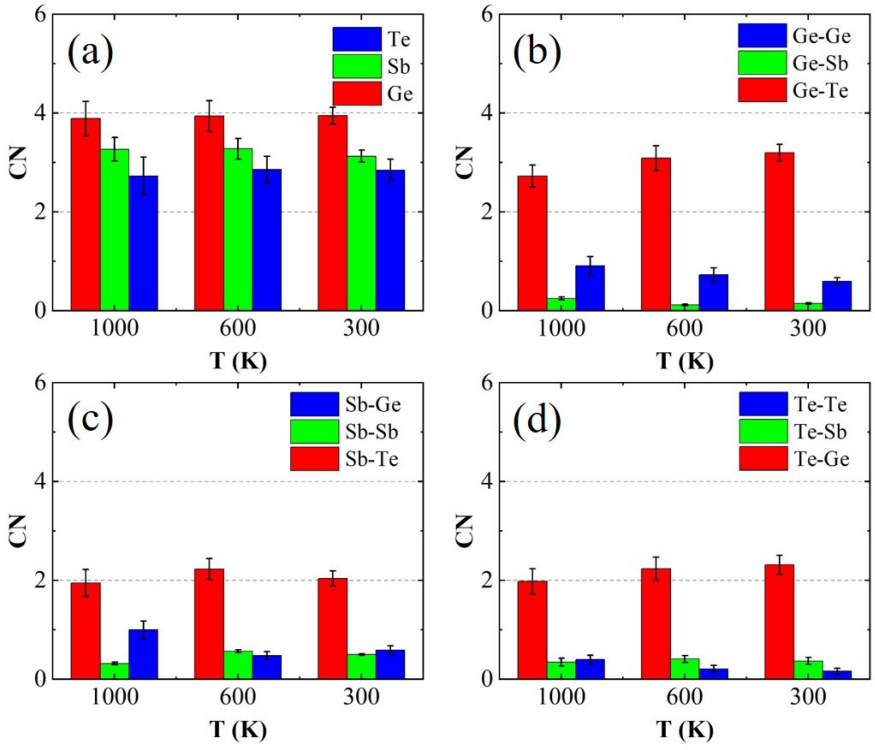

Fig. 2 The CN of different elements (a) in amorphous $Ge_8Sb_2Te_{11}$ at various temperatures, and (b)-(d) are the CN of specific configurations.

Fig. 3(a) shows the bond-angle distribution function (BADF) of amorphous $Ge_8Sb_2Te_{11}$ at different temperatures. At 1000 K, a principal peak is observed at ~90°, reminding us of the octahedral-like structures [39]. A small peak was found at ~58°, indicating the existence of the triangular configurations [42]. As the temperature decreases, the prominent peak is enhanced while the small peak is decreased, demonstrating that the octahedral configurations are enhanced while the triangular configurations are reduced in the amorphization process. In addition, a small peak appears at ~170°, which is usually ascribed to the distortions of the octahedral clusters.

The BADF of Ge-centered clusters is shown in Fig. 3(b). The main peak locates at ~90° at 1000 K, and a small peak is found at ~58°. As the temperature decreases to 300 K gradually, the main peak shifts to the right slightly and its height is increased, while the height of the small peak is decreased, and a new peak locating at ~170° is formed. Meanwhile, a shoulder peak located at 109° becomes more obvious in the amorphization process, suggesting the formation of tetrahedral-like structures. The BADF of Sb-centered clusters is shown in Fig. 3(c). Only one obvious peak is found at ~90° under 1000 K. With the decreasing temperature, the prominent peak is increased and shifts to right. The BADF of Te-centered clusters is shown in Fig. 3(d). At 1000 K, a main peak is observed at ~90°, and a small peak is observed at ~58°. As the temperature decreases, the main peak shifts to left and its height is enhanced, and the height of the small peak is reduced. Then it is inferred that all of Ge-, Sb- and Te-centered clusters are inclined to form the octahedral structures in amorphous $Ge_8Sb_2Te_{11}$, the triangular configurations are generated by both Ge- and Te-centered clusters, and the structural distortion of octahedron dominantly stems from the Ge-centered octahedrons.

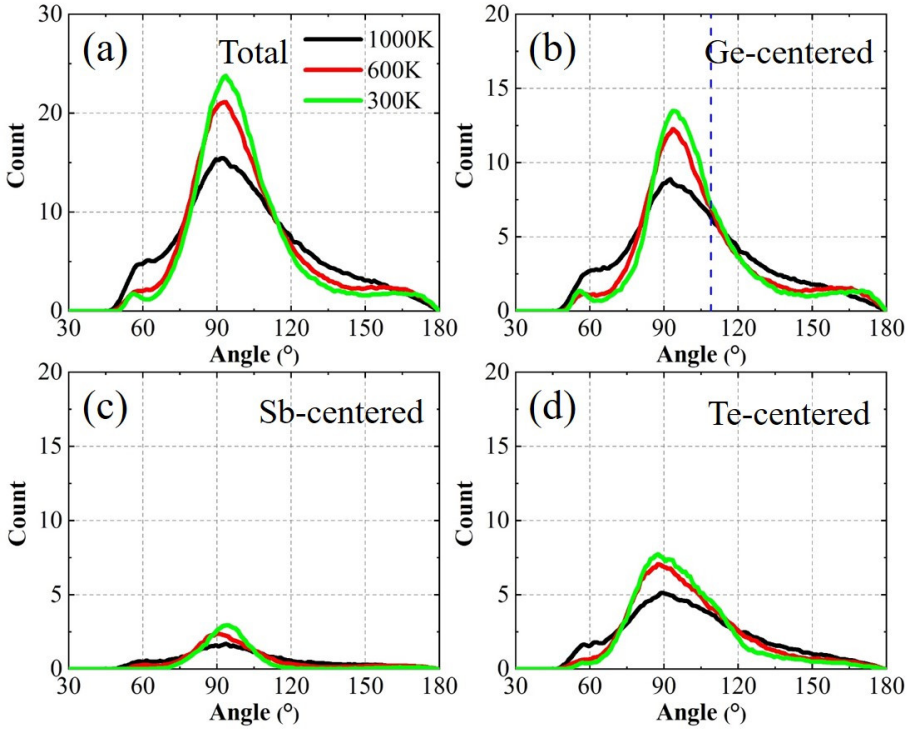

Fig. 3 The BADF of total (a), Ge-centered (b), Sb-centered (c) and Te-centered (d) configurations of amorphous $Ge_8Sb_2Te_{11}$ in the cooling process. The blue dashed line in (b) locates at 109°.

In amorphous phases of Ge-Sb-Te alloys, Ge-centered clusters also could form the tetrahedral structures in addition to the octahedral configurations [38,44], and the Ge-centered tetrahedrons play an important role in the stability of the amorphous state [9]. To quantify the Ge-centered tetrahedron in amorphous $Ge_8Sb_2Te_{11}$, the local structural order parameter q is applied [45-47],

$$q = 1 - \frac{3}{8}\sum_{i>k}\left(\frac{1}{3} + \cos\theta_{ijk}\right)^2 \quad (1)$$

in which the sum runs over the couple of atoms bonded to a central atom j. For the 4-coordinated clusters, when the q value of one cluster is equal to 1, it demonstrates that the cluster possesses an ideal tetrahedral structure. The smaller q value represents the larger difference between the selected cluster and the ideal tetrahedron. Usually, the clusters possessing the q values from 0.8 to 1.0 are seen as the tetrahedral patterns regardless of the distortions. The distribution of q of 4-coordinated Ge-centered clusters

is shown in Fig. 4(a). The peak of q values in the range of 0.8-1.0 is relatively small at 1000 K. As the temperature becomes 600K, the peak becomes prominent. When the temperature decreases to 300 K eventually, the height of the peak is further enhanced, and the peak shifts to right, indicating that the Ge-centered tetrahedrons are increased and these tetrahedrons become ordered in the amorphization process. By summing up the q values ranging from 0.8 to 1.0, the fractions of tetrahedrons in Ge-centered clusters are obtained, with the fractions of 10.9%, 21.8% and 30.4% at 1000 K, 600 K and 300 K, respectively. The fraction of tetrahedrons from AIMD simulation is smaller than the case from the CPMD program [19]. Comparing with the fractions in amorphous $Ge_2Sb_2Te_5$ (23.2%) and $Ge_3Sb_2Te_6$ (26.7%) [38], the fraction of tetrahedrons in amorphous $Ge_8Sb_2Te_{11}$ is larger. From Fig. 4(b), the Ge-centered tetrahedrons are randomly distributed in the amorphous $Ge_8Sb_2Te_{11}$. It is probably due to the large fraction of Ge-centered tetrahedrons and the random distribution of tetrahedrons that ensure amorphous $Ge_8Sb_2Te_{11}$ a high structural stability.

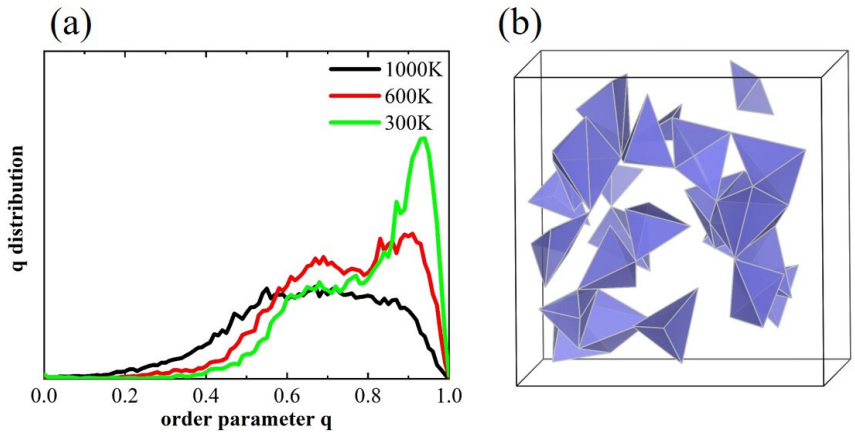

Fig. 4 The distribution of local order parameter q (a) for Ge-centered clusters with four-coordinated atoms, and the distribution of Ge-centered tetrahedrons (b) in simulated box.

The MRO is usually formed by the connection of the SRO in amorphous state. To explore the MRO in amorphous $Ge_8Sb_2Te_{11}$, the ring distribution is counted by using the RINGS code [48]. Fig. 5(a) shows the ring distribution of liquid $Ge_8Sb_2Te_{11}$ at 1000

K. 3-fold ring presents a fraction of 7.4%, 4-fold ring presents the largest fraction of 12.4%, 5-fold ring presents the fraction of 10.0%, 6-fold ring presents a fraction of 7.1%, and the fractions of larger rings are uniform. As the temperature decreases to 300 K, the fraction of 3-fold ring is decreased to 2.2%, indicating the triangular configuration is decreased in the amorphization process. The fraction of 4-fold ring is increased to 13.8% slightly while that of 6-fold ring is increased to 9.7%. As 4-fold and 6-fold rings are the important signature during the crystallization process [49], the large fractions of 4-fold and 6-fold rings could ensure the fast phase change from amorphous phase to crystalline phase. The 5-fold ring remains possessing a large fraction of 12.4% in amorphous $Ge_8Sb_2Te_{11}$. This is different from the other amorphous GeSbTe alloys obviously [46,49]. As 5-fold ring could hinder the crystallization of the amorphous state, thus amorphous $Ge_8Sb_2Te_{11}$ also presents a high stability. The large fractions of 12-fold to 16-fold rings are due to the formation of the nanocavities [50,51].

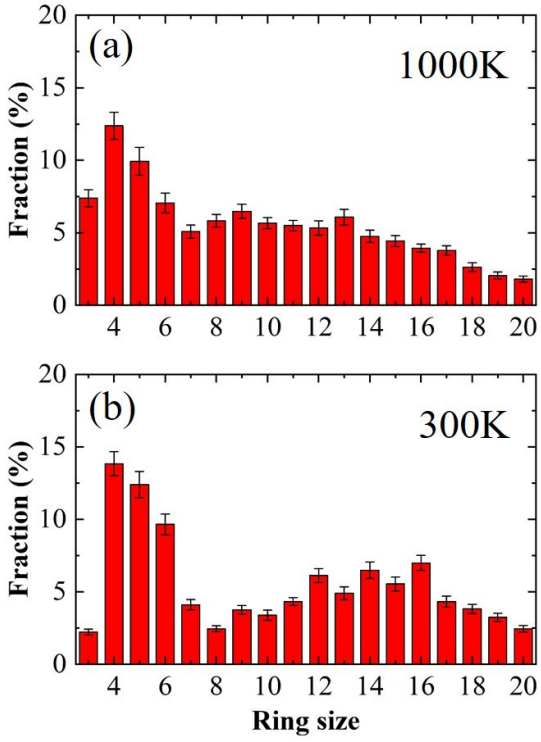

Fig. 5 The ring distributions of amorphous $Ge_8Sb_2Te_{11}$ at 1000 K (a) and 300 K (b) respectively.

Fig. 6(a) shows the mean square displacement (MSD) of amorphous $Ge_8Sb_2Te_{11}$ at different temperatures. The MSD decreases with the decreasing temperature, indicating that the atomic motion is reduced in the amorphization process. The velocity autocorrelation function (VACF) of amorphous $Ge_8Sb_2Te_{11}$ is shown in Fig. 6(b), which can reflect the atomic migration ability from the initial position. The curve of each element gradually converges to zero with time. The shorter time taking represents the stronger migration capacity of the atom. The convergence time of Ge, Sb and Te are about 0.55 ps, 1.43 ps and 1.20 ps, respectively, demonstrating that Ge atoms possess the largest migration capacity while Sb atoms possess the smallest migration capacity in amorphous $Ge_8Sb_2Te_{11}$.

By using the Fourier transform on VACF, the vibrational density of states (VDOS) of amorphous $Ge_8Sb_2Te_{11}$ at different temperatures are obtained, as shown in Fig. 6(c). At 1000 K, two distinct aggregation regions present in the VDOS, which can be named as the low frequency region (0-2.4 THz) and the high frequency region (2.4-6.7 THz). As the temperature decreases, the VDOS in low frequency region becomes more concentrated and the number is decreased, while the number of VDOS in high frequency region is obviously increased. It is demonstrated that the increment of VDOS in high frequency and the decrement of VDOS in low frequency will enhance the stability of the amorphous state in previous studies [52]. Thus, amorphous $Ge_8Sb_2Te_{11}$ becomes more stable in the amorphization process. Fig. 6(d)-(f) shows the VDOS of Ge, Sb and Te in the cooling process. The VDOS decreases in low frequency region while increases in the high frequency region for all of the three elements. Combining with the evolution of CN in Fig. 2, in which the CN of Ge-Ge decreases while Ge-Te increases for Ge-centered configurations, the CN of Sb-Ge decreases for Sb-centered configurations, and the CN of Te-Te decreases while Te-Ge increases for Te-centered configurations, it is inferred that the homopolar bonds may be the origin of the VDOS of low frequency while the heteropolar bonds contribute to the formation of the VDOS of high frequency.

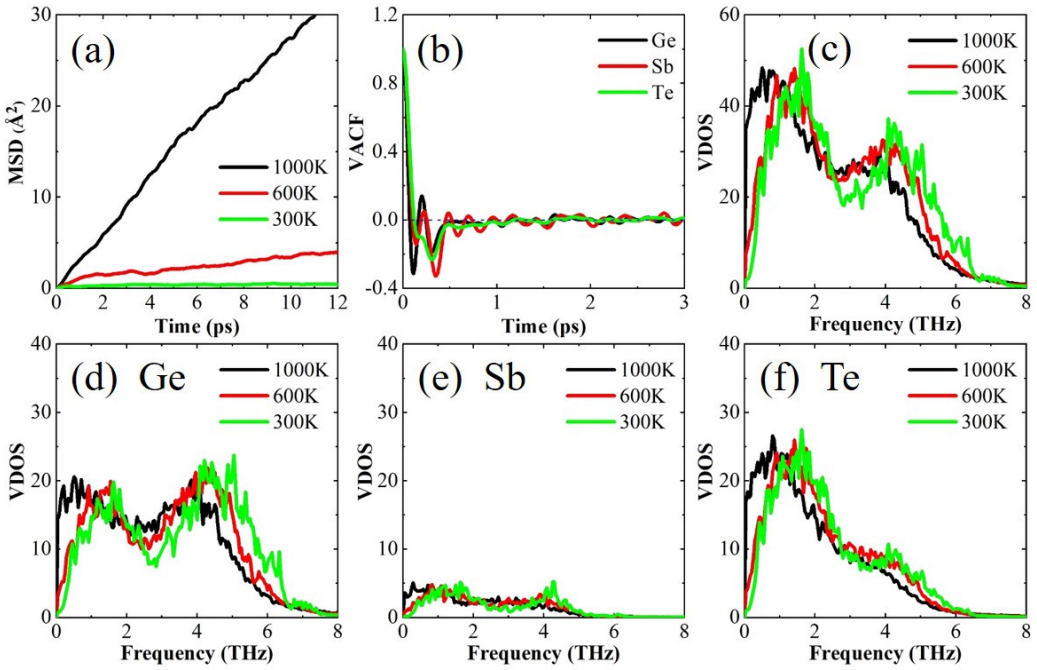

Fig. 6 (a) The MSD of $Ge_8Sb_2Te_{11}$ in the amorphization process, and (b) the VACF of amorphous $Ge_8Sb_2Te_{11}$ at 300 K. (c)-(f) The VDOS of total, Ge, Sb and Te atoms in amorphous $Ge_8Sb_2Te_{11}$ at different temperatures, respectively.

To further analyze the bonding characteristics in amorphous $Ge_8Sb_2Te_{11}$, the LOBSTER code is utilized to calculate the crystal orbital Hamilton populations (COHP) of different bonding configurations [53], as seen in Fig. 7(a). The -COHP of these bonds are negative below the Fermi level, suggesting that the antibonding interactions exist in these bonds. The -COHP of Sb-Sb and Te-Te bonds present the notable valleys in a large range, indicating that the antibonding interactions play an important role in these bonds. The -COHP of Ge-Te, Sb-Te, Ge-Ge and Ge-Sb bonds present the relatively small valleys, indicating that the antibonding interactions contribute little to these bonds.

By integrating the COHP below the Fermi level, the integrated COHP (ICOHP) can be obtained, which reflects the formation energy of the corresponding bonding configurations. Fig. 7(b) shows the -ICOHP of different bonding configurations in amorphous $Ge_8Sb_2Te_{11}$ at 0 K. in which the two dashed lines are corresponding to the two peaks in g(r). The formation energies decrease with the increasing distance,

illustrating that the longer the bonding distance the weaker the bonding strength. At the vicinity of 2.79 Å, the formation energies of Ge-Te and Sb-Te bonds are 2.81 eV and 3.35 eV, respectively. This is in line with the experimental result where certifies that the Sb-Te bond is stiffer than the Ge-Te bond [54]. The -ICOHP of Ge-Te bond is larger than Ge-Ge bond, and the -ICOHP of Sb-Te bond is larger than Ge-Sb, Sb-Sb and Te-Te bonds, illustrating that Ge-Te bond is stronger than Ge-Ge bond and Sb-Te bond is stronger than Ge-Sb, Sb-Sb and Te-Te bonds. This is the reason why amorphous $Ge_8Sb_2Te_{11}$ tends to form the ABAB bonding alternations. At ~4.18 Å, the bonding configurations are corresponding to the atoms in second shell, and the -ICOHP is relatively small because of the large distance. It is possibly due to the small interactions that lead to the weak MRO.

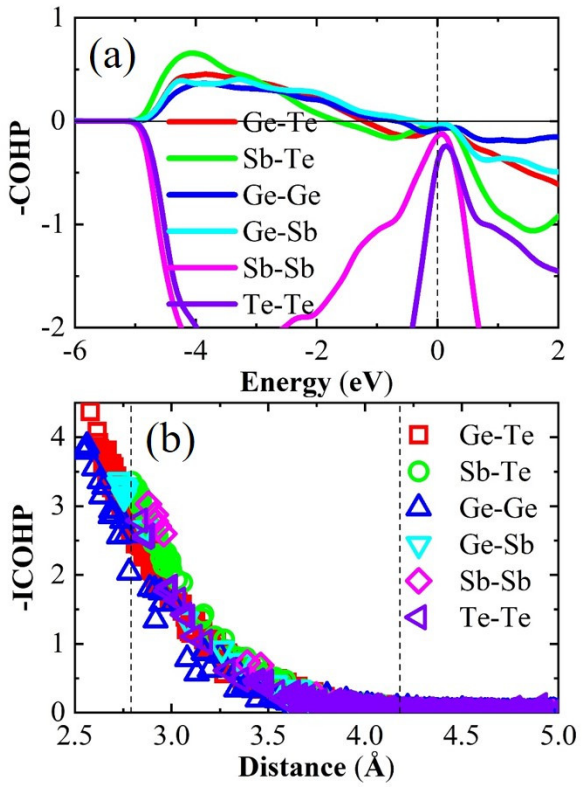

Fig. 7 The -COHP (a) and –ICOHP (b) of different bonding configurations in the amorphous $Ge_8Sb_2Te_{11}$.

The density of states (DOS) and inverse participation ratio (IPR) of amorphous

$Ge_8Sb_2Te_{11}$ are shown in Fig. 8(a). The valence band and conduction band are dominantly contributed by the Ge and Te elements, this is because of their large content in amorphous $Ge_8Sb_2Te_{11}$. The mid-gap states are also observed in the bandgap of DOS, and most of them originate from the Ge and Te atoms, this is usually ascribed to the over-coordinated structures of Ge-centered and Te-centered configurations [33,34,55]. To reduce the effect of band tail on the bandgap, the IPR is used to evaluate the bandgap (also known as the mobility bandgap in glasses) [56], which identifies the locations of valence band maximum and conduction band minimum by the relatively larger IPR values (marked with the dashed line in Fig. 8(a)). The calculated bandgap of amorphous $Ge_8Sb_2Te_{11}$ is ~ 0.7 eV, which is in line with the previous simulated value [19] and a little smaller than the experimental optical energy gaps [24,25,27,57-59]. Fig. 8(b) shows the projected DOS of amorphous $Ge_8Sb_2Te_{11}$. Due to the little contribution, the d states of Ge, Sb and Te atoms are not shown in the PDOS. Near the valence band maximum, the p state of Ge, Sb and Te possess a large amount, indicating that these atoms tend to form the σ bonds. In addition, the s state of Ge atoms also possesses a large fraction, hinting the formation of sp^3 hybrid bond (i.e., Ge-centered tetrahedron).

Fig. 8(c) plots the distribution curve of normalized electron localized function (ELF). The electrons in the covalent bond are completely localized at ELF=1.0, while the electrons in the metallic bond are completely delocalized at ELF=0.5. The main peak observed at 0.85 suggests the electrons are partially localized. The fraction of lone-pair electrons is obtained by integrating the ELF values from 0.85 to 1.0 [60]. The calculated fraction is about 14.8% in amorphous $Ge_8Sb_2Te_{11}$, which is larger than the case (10.0%) in pure amorphous Te [34]. The snapshot of ELF is shown in Fig. 8(d), with an isovalue of 0.9. The lone-pair electrons can be visualized by the orange isosurfaces locating at the other side of the bonding region. The existence of lone pair electrons leads to the asymmetry of bonding configurations in defective octahedral configurations, thus the larger fraction of lone pair electrons will lead to more disordered local structures.

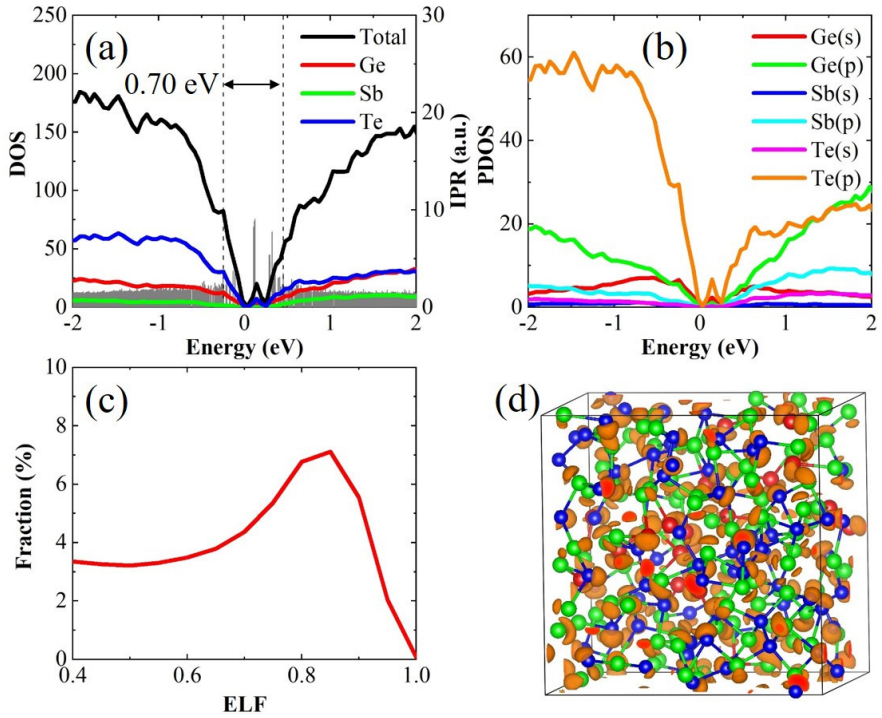

Fig. 8 The DOS and IPR (a), PDOS (b) and distribution of ELF (c) of the amorphous $Ge_8Sb_2Te_{11}$. (d) The distribution of ELF in the simulated cell, with an isosurface of 0.9, where blue, pink and green balls represent the Ge, Sb and Te atoms.

Conclusions

In summary, the AIMD simulations were utilized to explore the structure evolution of amorphous $Ge_8Sb_2Te_{11}$ in the cooling process, and the first principles calculations were utilized to study the bonding and electronic properties. The results indicate that both the SRO and MRO are enhanced in the melt-quenching process. For the SRO, most of the Ge-, Sb- and Te-centered clusters are mainly in the form of octahedral structures with distortions in amorphous $Ge_8Sb_2Te_{11}$. While 30.4% of Ge-centered clusters also form the tetrahedral configurations, and they are randomly distributed in the amorphous system. As for the MRO, in addition to 4-fold and 6-fold rings, the 5-fold rings, which could prevent the crystallization behavior, also possess a large fraction in amorphous $Ge_8Sb_2Te_{11}$. During the cooling process, the VDOS of Ge, Sb and Te atoms decrease in the low frequency region but increase in the high frequency region, indicating that the stable bonding configurations are increased in the amorphization process. The Ge-Te

and Sb-Te bonds present larger formation energies, making the formation of ABAB bonds in amorphous $Ge_8Sb_2Te_{11}$. The fraction of lone pair electrons is ~14.8%, which are usually located at the opposite direction of bonds, thus could enhance the distortions of the SRO. It is probably due to the large fraction of tetrahedrons, 5-fold rings, strong ABAB bonding sequence and larger distortions that make amorphous $Ge_8Sb_2Te_{11}$ a high stable glass. Our research findings provide an in-depth understanding of the structure and electronic properties of amorphous $Ge_8Sb_2Te_{11}$, which can promote the applications to optical phase-change memory.

Acknowledgements

The work was partially supported by the National Science and Technology Major Project of China (Grant No. 2022ZD0117600). C.Q. acknowledges the Doctoral Research Foundation of Nanyang Institute of Technology and Research Center of Mathematics and Applied Mathematics. S.Z.W. acknowledges the Science and Technology Department of Henan Province (No. 212102210464). C.C. acknowledges the Natural Science Foundation of Jiangsu Higher Education Institutions of China (Grant No. 22KJB140003). M.X. acknowledges the National Natural Science Foundation of China (Grant No. 62174060) and Hubei Key Laboratory of Advanced Memories. Work at Ames Laboratory was supported by the U.S. Department of Energy (DOE), Office of Science, Basic Energy Sciences, Materials Science and Engineering Division including a grant of computer time at the National Energy Research Scientific Computing Centre (NERSC) in Berkeley, CA. Ames Laboratory is operated for the U.S. DOE by Iowa State University under Contract No. DE-AC02-07CH11358.

References

[1] M. Lanza, A. Sebastian, W.D. Lu, M. Le Gallo, M.-F. Chang, D. Akinwande, F.M. Puglisi, H.N. Alshareef, M. Liu, J.B. Roldan, Memristive technologies for data storage, computation, encryption, and radio-frequency communication, Science 376 (2022) 1066.

[2] W. Zhang, R. Mazzarello, M. Wuttig, E. Ma, Designing crystallization in phase-change materials for universal memory and neuro-inspired computing, Nat. Rev. Mater. 4 (2019) 150-168.

[3] Y.-T. Liu, X.-B. Li, H. Zheng, N.-K. Chen, X.-P. Wang, X.-L. Zhang, H.-B. Sun, S. Zhang, High-Throughput Screening for Phase-Change Memory Materials, Adv. Funct. Mater. 31 (2021) 2009803.

[4] M. Wuttig, H. Bhaskaran, T. Taubner, Phase-change materials for non-volatile photonic applications, Nat. Photonics 11 (2017) 465-476.

[5] M. Xu, M. Xu, X. Miao, Deep machine learning unravels the structural origin of mid-gap states in chalcogenide glass for high-density memory integration, Infomat 4 (2022) e12315.

[6] M. Xu, Q. Xu, R. Gu, S. Wang, C.-Z. Wang, K.-M. Ho, Z. Wang, M. Xu, X. Miao, Tailoring Mid-Gap States of Chalcogenide Glass by Pressure-Induced Hypervalent Bonding Towards the Design of Electrical Switching Materials, Adv. Funct. Mater. 33 (2023) 2304926.

[7] Z. Sun, J. Zhou, A. Blomqvist, B. Johansson, R. Ahuja, Formation of Large Voids in the Amorphous Phase-Change Memory $Ge_2Sb_2Te_5$ Alloy, Phys. Rev. Lett. 102 (2009) 075504.

[8] F. Rao, K. Ding, Y. Zhou, Y. Zheng, M. Xia, S. Lv, Z. Song, S. Feng, I. Ronneberger, R. Mazzarello, W. Zhang, E. Ma, Reducing the stochasticity of crystal nucleation to enable subnanosecond memory writing, Science 358 (2017) 1423-1426.

[9] J.Y. Raty, W. Zhang, J. Luckas, C. Chen, R. Mazzarello, C. Bichara, M. Wuttig, Aging mechanisms in amorphous phase-change materials, Nat. Commun. 6 (2015) 7467.

[10] T. Matsunaga, N. Yamada, Structural investigation of $GeSb_2Te_4$: A high-speed phase-change material, Physical Review B 69 (2004) 104111.

[11] D. Loke, T.H. Lee, W.J. Wang, L.P. Shi, R. Zhao, Y.C. Yeo, T.C. Chong, S.R. Elliott, Breaking the Speed Limits of Phase-Change Memory, Science 336 (2012) 1566-1569.

[12] A.-K.U. Michel, M. Wuttig, T. Taubner, Design Parameters for Phase-Change Materials for Nanostructure Resonance Tuning, Adv. Opt. Mater. 5 (2017) 1700261.

[13] M. Bouska, S. Pechev, Q. Simon, R. Boidin, V. Nazabal, J. Gutwirth, E. Baudet, P. Nemec, Pulsed laser deposited GeTe-rich GeTe-Sb_2Te_3 thin films, Sci. Rep. 6 (2016) 26552.

[14] C. Chen, C. Qiao, M. Xu, X. Miao, Temperature dependent dielectric properties of GeTe-rich $(GeTe)_x(Sb_2Te_3)_{1-x}$ glass, Appl. Phys. Lett. 121 (2022) 212103.

[15] T. Matsunaga, H. Morita, R. Kojima, N. Yamada, K. Kifune, Y. Kubota, Y. Tabata, J.J. Kim, M. Kobata, E. Ikenaga, K. Kobayashi, Structural characteristics of GeTe-rich GeTe-Sb_2Te_3 pseudobinary metastable crystals, J. Appl. Phys. 103 (2008) 093511.

[16] P. Zalden, C. Koch, M. Paulsen, M. Esters, D.C. Johnson, M. Wuttig, A.M. Lindenberg, W. Bensch, Acceleration of Crystallization Kinetics in Ge-Sb-Te-Based Phase-Change Materials by Substitution of Ge by Sn, Adv. Funct. Mater. 31 (2021) 2004803.

[17] M. Wuttig, D. Luesebrink, D. Wamwangi, W. Welnic, M. Gillessen, R. Dronskowski, The role of vacancies and local distortions in the design of new phase-change materials, Nat. Mater. 6 (2007) 122.
[18] B.J. Kooi, M. Wuttig, Chalcogenides by Design: Functionality through Metavalent Bonding and Confinement, Adv. Mater. 32 (2020) 1908302.
[19] J. Akola, R.O. Jones, Structure of amorphous $Ge_8Sb_2Te_{11}$: GeTe-Sb_2Te_3 alloys and optical storage, Phys. Rev. B 79 (2009) 134118.
[20] T.H. Lee, S.R. Elliott, Ab Initio Computer Simulation of the Early Stages of Crystallization: Application to $Ge_2Sb_2Te_5$ Phase-Change Materials, Phys. Rev. Lett. 107 (2011) 145702.
[21] J. Akola, J. Larrucea, R.O. Jones, Polymorphism in phase-change materials: melt-quenched and as-deposited amorphous structures in $Ge_2Sb_2Te_5$ from density functional calculations, Phys. Rev. B 83 (2011) 094113.
[22] M. Krbal, A.V. Kolobov, P. Fons, J. Tominaga, S.R. Elliott, J. Hegedus, T. Uruga, Intrinsic complexity of the melt-quenched amorphous $Ge_2Sb_2Te_5$ memory alloy, Phys. Rev. B 83 (2011) 054203.
[23] M. Krbal, J. Bartak, J. Kolar, A. Prytuliak, A.V. Kolobov, P. Fons, L. Bezacier, M. Hanfland, J. Tominaga, Pressure-Induced Phase Transitions in GeTe-Rich Ge-Sb-Te Alloys across the Rhombohedral-to-Cubic Transitions, Inorg. Chem. 56 (2017) 7687-7693.
[24] S.-W. Kim, W.-S. Lim, T.-W. Kim, H.-Y. Lee, Influence of hydrogenation on the amorphous-to-crystalline phase transition characteristics of $Ge_2Sb_2Te_5$ and $Ge_8Sb_2Te_{11}$ thin films, Jpn. J. Appl. Phys. 47 (2008) 5337-5341.
[25] K.-H. Song, S.-W. Kim, J.-H. Seo, H.-Y. Lee, Influence of the additive Ag for crystallization of amorphous Ge-Sb-Te thin films, Thin Solid Films 517 (2009) 3958-3962.
[26] C. Koch, T. Dankwort, A.-L. Hansen, M. Esters, D. Haeussler, H. Volker, A. von Hoegen, M. Wuttig, D.C. Johnson, W. Bensch, L. Kienle, Investigation of the phase change mechanism of $Ge_6Sn_2Sb_2Te_{11}$, Acta Mater. 152 (2018) 278-287.
[27] S. Buller, C. Koch, W. Bensch, P. Zalden, R. Sittner, S. Kremers, M. Wuttig, U. Schuermann, L. Kienle, T. Leichtweiss, J. Janek, B. Schoenborn, Influence of Partial Substitution of Te by Se and Ge by Sn on the Properties of the Blu-ray Phase-Change Material $Ge_8Sb_2Te_{11}$, Chem. Mater. 24 (2012) 3582-3590.
[28] J. Wang, Q. Li, S. Tao, Z. Xia, Y. Li, Y. Liu, Z. Gu, C. Hu, Improving the reflectance and color contrasts of phase-change materials by vacancy reduction for optical-storage and display applications, Opt. Lett. 45 (2020) 244-247.
[29] G. Kresse, J. Hafner, Ab initio molecular dynamics for liquid metals, Phys. Rev. B 47 (1993) 558-561.
[30] G. Kresse, J. Furthmuller, Efficient iterative schemes for ab initio total-energy calculations using a plane-wave basis set, Phys. Rev. B 54 (1996) 11169-11186.
[31] P.E. Blochl, Projector augmented-wave method, Phys. Rev. B 50 (1994) 17953-17979.
[32] J.P. Perdew, K. Burke, M. Ernzerhof, Generalized gradient approximation made simple, Phys. Rev. Lett. 78 (1997) 1396-1396.

[33] C. Qiao, S. Wang, L. Chen, B. Liu, S. Bai, R. Gu, S. Wang, C.-Z. Wang, K.-M. Ho, X. Miao, M. Xu, Unveiling the structure and electronic characteristics of amorphous GeS for high performance threshold switching, Appl. Phys. Lett. 123 (2023) 112107.
[34] C. Qiao, M. Xu, S. Wang, C.-Z. Wang, K.-M. Ho, X. Miao, M. Xu, Structure, bonding nature and transition dynamics of amorphous Te, Scr. Mater. 202 (2021) 114011.
[35] C. Qiao, Y.R. Guo, F. Dong, J.J. Wang, H. Shen, S.Y. Wang, M. Xu, X.S. Miao, Y.X. Zheng, R.J. Zhang, L.Y. Chen, C.Z. Wang, K.M. Ho, Evolution of short- and medium-range order in the melt-quenching amorphization of $Ge_2Sb_2Te_5$, J. Mater. Chem. C 6 (2018) 5001-5011.
[36] S. Nose, A unified formulation of the constant temperature molecular dynamics methods, J. Chem. Phys. 81 (1984) 511-519.
[37] W.G. Hoover, Canonical dynamics: Equilibrium phase-space distributions, Phys. Rev. A 31 (1985) 1695-1697.
[38] C. Qiao, Y.R. Guo, J.J. Wang, H. Shen, S.Y. Wang, Y.X. Zheng, R.J. Zhang, L.Y. Chen, C.Z. Wang, K.M. Ho, The local structural differences in amorphous Ge-Sb-Te alloys, J. Alloys Compd. 774 (2019) 748-757.
[39] Z. Sun, J. Zhou, A. Blomqvist, B. Johansson, R. Ahuja, Fast crystallization of chalcogenide glass for rewritable memories, Appl. Phys. Lett. 93 (2008) 061913.
[40] J. Kalikka, J. Akola, J. Larrucea, R.O. Jones, Nucleus-driven crystallization of amorphous $Ge_2Sb_2Te_5$: A density functional study, Phys. Rev. B 86 (2012) 144113.
[41] P. Jovari, I. Kaban, J. Steiner, B. Beuneu, A. Schops, A. Webb, 'Wrong bonds' in sputtered amorphous $Ge_2Sb_2Te_5$, J. Phys.: Condens. Matter 19 (2007) 335212.
[42] J. Akola, R.O. Jones, Density functional study of amorphous, liquid and crystalline $Ge_2Sb_2Te_5$: homopolar bonds and/or AB alternation?, J. Phys.: Condens. Matter 20 (2008) 465103.
[43] N.-K. Chen, X.-B. Li, X.-P. Wang, W.Q. Tian, S. Zhang, H.-B. Sun, Strong electron-polarized atom chain in amorphous phase-change memory Ge-Sb-Te alloy, Acta Mater. 143 (2018) 102-106.
[44] S. Caravati, M. Bernasconi, T.D. K hne, M. Krack, M. Parrinello, Coexistence of tetrahedral- and octahedral-like sites in amorphous phase change materials, Appl. Phys. Lett. 91 (2007) 171906.
[45] J.R. Errington, P.G. Debenedetti, Relationship between structural order and the anomalies of liquid water, Nature 409 (2001) 318-321.
[46] C. Qiao, K. Bai, M. Xu, S. Wang, C.-Z. Wang, K.-M. Ho, X. Miao, M. Xu, Ultrafast crystallization mechanism of amorphous $Ge_{15}Sb_{85}$ unraveled by pressure-driven simulations, Acta Mater. 216 (2021) 117123.
[47] A. Bouzid, G. Ori, M. Boero, E. Lampin, C. Massobrio, Atomic-scale structure of the glassy $Ge_2Sb_2Te_5$ phase change material: A quantitative assessment via first-principles molecular dynamics, Phys. Rev. B 96 (2017) 224204.
[48] S. Le Roux, P. Jund, Ring statistics analysis of topological networks: New

approach and application to amorphous GeS_2 and SiO_2 systems, Comp. Mater. Sci. 49 (2010) 70-83.

[49] J. Hegedus, S.R. Elliott, Microscopic origin of the fast crystallization ability of Ge-Sb-Te phase-change memory materials, Nat. Mater. 7 (2008) 399-405.

[50] S. Caravati, M. Bernasconi, M. Parrinello, First-principles study of liquid and amorphous Sb_2Te_3, Phys. Rev. B 81 (2010) 014201.

[51] J. Akola, R.O. Jones, Structural phase transitions on the nanoscale:: The crucial pattern in the phase-change materials $Ge_2Sb_2Te_5$ and GeTe, Phys. Rev. B 76 (2007) 235201.

[52] J.-Y. Raty, P. Noe, G. Ghezzi, S. Maitrejean, C. Bichara, F. Hippert, Vibrational properties and stabilization mechanism of the amorphous phase of doped GeTe, Phys. Rev. B 88 (2013) 014203.

[53] R. Nelson, C. Ertural, J. George, V.L. Deringer, G. Hautier, R. Dronskowski, LOBSTER: Local orbital projections, atomic charges, and chemical-bonding analysis fromprojector-augmented-wave-baseddensity-functional theory, J. Comput. Chem. 41 (2020) 1931-1940.

[54] M. Krbal, A.V. Kolobov, P. Fons, R.E. Simpson, T. Matsunaga, J. Tominaga, N. Yamada, Local atomic order of crystalline $Ge_8Sb_2Te_{11}$ across the ferroelectric to paraelectric transition: The role of vacancies and static disorder, Phys. Rev. B 84 (2011) 104106.

[55] K. Konstantinou, F.C. Mocanu, T.-N. Lee, S.R. Elliott, Revealing the intrinsic nature of the mid-gap defects in amorphous $Ge_2Sb_2Te_5$, Nat. Commun. 10 (2019) 3065.

[56] S. Jia, H. Li, T. Gotoh, C. Longeaud, B. Zhang, J. Lyu, S. Lv, M. Zhu, Z. Song, Q. Liu, J. Robertson, M. Liu, Ultrahigh drive current and large selectivity in GeS selector, Nat. Commun. 11 (2020) 4636.

[57] K.-H. Song, S.-C. Baek, H.-Y. Lee, Amorphous-to-crystalline phase transformation in $(GeTe)_x(Sb_2Te_3)$ (x = 0.5, 1, 2, 8) thin films, J. Korean Phys. Soc. 61 (2012) 10-16.

[58] C.-J. Park, H. Kong, H.-Y. Lee, J.-B. Yeo, Effect of tungsten on the phase-change properties of $Ge_8Sb_2Te_{11}$ thin films for the phase-change device, J. Korean Phys. Soc. 71 (2017) 42-46.

[59] Y. Zhang, Y. Zhang, R. Song, J. Ma, L. Wu, L. Song, High thermal stability and optical contrast of Mo-doped $Ge_8Sb_2Te_{11}$ films prepared by magnetron co-sputtering, Ceram. Int. 49 (2023) 40105- 40111.

[60] J.-Y. Raty, C. Gatti, C.-F. Schoen, M. Wuttig, How to Identify Lone Pairs, Van der Waals Gaps, and Metavalent Bonding Using Charge and Pair Density Methods: From Elemental Chalcogens to Lead Chalcogenides and Phase-Change Materials, Phys. Status Solidi RRL 15 (2021) 2000534.